Dalton Transactions

ROYAL SOCIETY OF CHEMISTRY

PAPER

View Article Online
View Journal | View Issue

Cite this: *Dalton Trans.*, 2024, **53**, 9294

Borylation and rearrangement reactions of azasilaanthracenes to afford B,N-doped nanographenes†

Elena Zender,[a] Danillo Valverde,[b] Robert Neubaur,[a] Sebastian Karger,[a] Alexander Virovets,[a] Michael Bolte,[a] Hans-Wolfram Lerner,[a] Yoann Olivier *[b] and Matthias Wagner *[a]

An air-stable B_3,N_3-containing dibenzobisanthene (**8**) was prepared in 29% yield by heating a 1,3,5-tri(azasilaanthryl)benzene (**5**) with BBr_3 (180 °C). Under these conditions, the reaction does not stop after threefold $SiMe_2$/BBr exchange but proceeds further *via* two rearrangement and two intramolecular C–H borylation steps. Some mechanistic details were unveiled by using smaller model systems and applying lower reaction temperatures. According to X-ray crystallography, compound **8** has a helically distorted scaffold. Due to its multiple resonance structure, it shows a narrow-band blue-green emission (λ_{em} = 493 nm; Φ_{PL} = 84%; FWHM = 0.20 eV; THF); samples measured in PMMA gave prompt and delayed fluorescence lifetimes of 10.7 ns and 136 µs, respectively. The optical properties of **8** and of structurally related species were also investigated by quantum-chemical means: most of these compounds exhibit a small energy gap ΔE_{ST} between the lowest excited singlet (S_1) and triplet (T_1) states and a non-negligible spin–orbit coupling (SOC) between S_1 and T_1/T_2, demonstrating their potential as thermally activated delayed fluorescence (TADF) emitters.

Received 19th April 2024,
Accepted 8th May 2024

DOI: 10.1039/d4dt01166j

rsc.li/dalton

Introduction

Polycyclic aromatic hydrocarbons (PAHs) containing π-electron-accepting B atoms and π-electron-donating N atoms in mutual 1,4-positions find increasing applications as OLED materials.[1] The main reason is that such heteroatom doping patterns can lead to a decoupling of the PAH's frontier orbitals, which, in turn, results in a small energy gap (ΔE_{ST}) between the lowest excited singlet and triplet states, facilitating triplet-to-singlet upconversion. As a consequence, corresponding B_n,N_m-PAHs are ideal candidates for use as MR-TADF emitters (MR-TADF: multiple resonance thermally activated delayed fluorescence). In theory, MR-TADF compounds can utilize all electrogenerated excitons in an OLED for luminescence, whereas conventional fluorescence emitters are only driven by the 25% of singlet excitons.[2–8] In terms of synthesis, many representatives of MR-TADF B_n,N_m-PAHs are notable for their convenient accessibility from suitable aryl amines through electrophilic aromatic borylation with BX_3 (X = Br, I).[3,9–12] We recently contributed to this field the B_3,N_2-PAH **C** (Scheme 1), which is one of the few examples that contain more B than N atoms and thus have a formally electron-deficient π system.[13] Remarkably, in this case the established threefold electrophilic C–H borylation failed for the introduction of the central B atom. Therefore, we had to use the halogenated starting materials **A** (X = Cl) or **B** (X = I) and form the first of the three B–C bonds (marked in red) *via* a lithiation/borylation approach.[2,13–17] Herein, we show that no **C** is

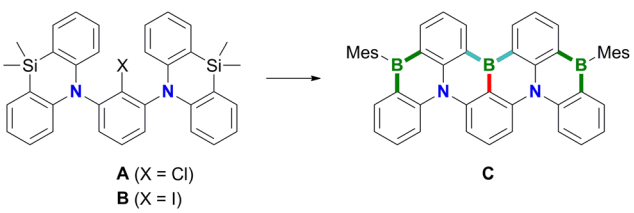

A (X = Cl)
B (X = I)

C

Scheme 1 The B_3,N_2-PAH **C** was synthesized from **A** or **B** *via* a sequence of lithiation/borylation (red bond), electrophilic aromatic borylation (blue bonds), and Si/B-exchange reactions (green bonds).

[a]*Institut für Anorganische und Analytische Chemie, Goethe-Universität Frankfurt, Max-von-Laue-Straße 7, D-60438 Frankfurt (Main), Germany. E-mail: matthias.wagner@chemie.uni-frankfurt.de*
[b]*Laboratory for Computational Modeling of Functional Materials, Namur Institute of Structured Matter, University of Namur, Rue de Bruxelles, 61, 5000 Namur, Belgium. E-mail: yoann.olivier@unamur.be*

†Electronic supplementary information (ESI) available: Experimental, analytical, computational, and crystallographic data. CCDC 2338843–2338851. For ESI and crystallographic data in CIF or other electronic format see DOI: https://doi.org/10.1039/d4dt01166j

formed in the reaction of parent **1** (X = H) with BBr_3, because a skeletal rearrangement to the ladder-type azaborine[1] $\mathbf{2^{Br}}$ takes place instead (Scheme 2). We provide insight into some mechanistic details of this rearrangement and expand the scope of the reaction from the 1,3-disubstituted precursor **1** to its 1,3,5-trisubstituted congener **5** (Scheme 3).

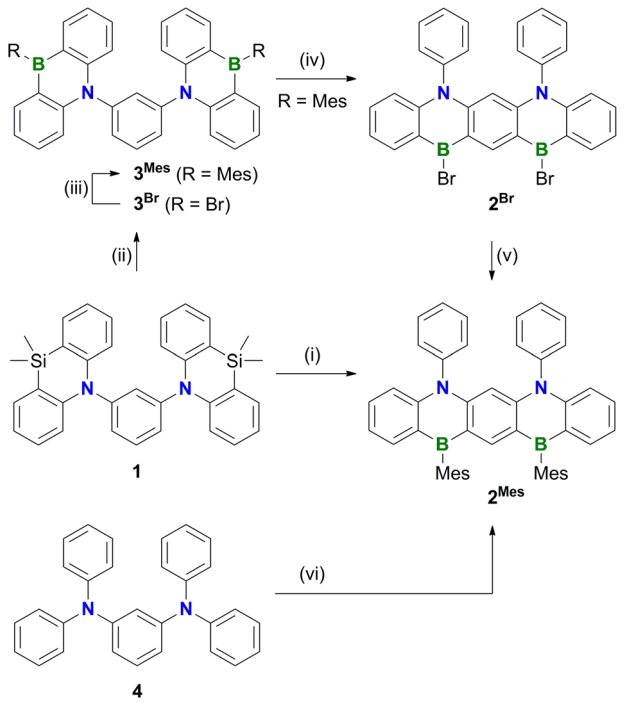

Scheme 2 Synthetic pathways to $\mathbf{2^{Mes}}$. Conditions: (i) 1. BBr_3 (12 equiv.), C_6H_6, 180 °C, 116 h, sealed ampoule; 2. MesMgBr (3 equiv.), toluene, −78 °C to room temperature, 39% over two steps; (ii) BBr_3 (5 equiv.), CH_2Cl_2, room temperature, 1 d, closed J. Young vessel, product was used after solvent exchange without further purification; (iii) MesMgBr (3 equiv. relative to **1**), toluene, −78 °C to room temperature, 42% over two steps; (iv) BBr_3 (12 equiv.), C_6H_6, 180 °C, 92 h, sealed ampoule, product was used after solvent exchange without further purification; (v) MesMgBr (3 equiv. relative to $\mathbf{3^{Mes}}$), toluene, −78 °C to room temperature, 44% over two steps; (vi) 1. BBr_3 (12 equiv.), *o*-dichlorobenzene, 180 °C, 112 h, sealed ampoule; 2. MesMgBr (3 equiv.), toluene, −78 °C to room temperature, 58% over two steps.

Results and discussion

Treatment of **1** with excess BBr_3 in C_6H_6 (12 equiv., 180 °C, 116 h) results in the formation of a characteristically red precipitate. Mesitylation of this primary product with MesMgBr affords $\mathbf{2^{Mes}}$ in 39% overall yield (Mes: mesityl; Scheme 2). Compound $\mathbf{2^{Mes}}$ was characterized by NMR spectroscopy, X-ray crystallography (Fig. S61†), and optoelectronic measurements (see below). Closely related B_2,N_2-pentacenes containing N–CH_2Ph or N–Me and aryl–*n*Bu moieties are known, but have been prepared from tetrabrominated *m*-phenylene diamines.[18–20] To gain insight into the mechanism underlying the formation of $\mathbf{2^{Mes}}$, **1** was stirred with BBr_3 (5 equiv.) in CH_2Cl_2 at room temperature; subsequent mesitylation gave $\mathbf{3^{Mes}}$ in 42% yield. This suggests that its B–Br precursor $\mathbf{3^{Br}}$ is likely present to a significant extent also during the synthesis of $\mathbf{2^{Mes}}$ before the red B_2,N_2-pentacene $\mathbf{2^{Br}}$ precipitates. Consistent with the postulated role of $\mathbf{3^{Br}}$ as a key intermediate, $\mathbf{2^{Br}}$ is also accessible from $\mathbf{3^{Mes}}$ and BBr_3 *via* an initial demesitylation[21] step (Fig. S1†). Overall, our experimental observations agree with quantum-chemical calculations (SMD(C_6H_6)/ωB97XD/def2-TZVP//SMD(C_6H_6)/ωB97XD/def2-SVP), which predict that $\mathbf{3^{Br}}$ is less stable by 4.3 kcal mol^{-1} than its ladder-type isomer $\mathbf{2^{Br}}$ (see the ESI† for more details). We finally emphasize that if the focus is not on the reactivity of **1** but on the preparation of $\mathbf{2^{Mes}}$, it is advisable to subject the readily available diamine **4** to C–H borylation with BBr_3, as this protocol gives a yield of 58%.

In an attempt to prepare larger B_n,N_m-doped PAHs, the protocol of the reaction $\mathbf{1} \rightarrow \mathbf{2^{Mes}}$ was subsequently adapted to tri(azasilaanthryl)benzene **5** (Scheme 3). Again, the borylation step in C_6H_6 led to the precipitation of a red solid, which was isolated and mesitylated. Besides $\mathbf{2^{Mes}}$, which stems from

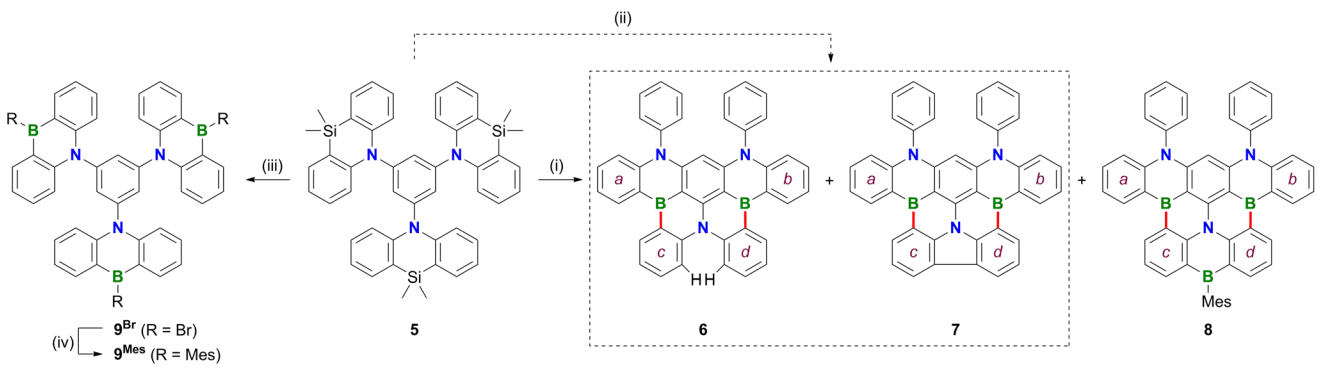

Scheme 3 Borylation and rearrangement reactions of **5**. Conditions: (i) 1. BBr_3 (28 equiv.), C_6H_6, 180 °C, 7 d, sealed ampoule; 2. MesMgBr (6 equiv.), toluene, −78 °C to room temperature, the product mixture contained **6**–**8**, but only **8** could be isolated in 29% yield over two steps; (ii) 1. BBr_3 (30 equiv.), C_6H_6, 180 °C, 11 d, sealed ampoule; 2. *i*PrOH, CH_2Cl_2, 6% (**6**), 9% (**7**); (iii) BBr_3 (neat), room temperature, 1 d, closed J. Young vessel, product was used after solvent exchange without further purification; (iv) MesMgBr (5 equiv. relative to **5**), toluene, −78 °C to room temperature, 56% over two steps.

unwanted C–N-bond cleavage,[22] the resulting product mixture included **6**, **7**, and **8** (the latter was isolated in 29% yield). To suppress the formation of **8** and $\mathbf{2}^{\mathbf{Mes}}$ and to obtain pure **6** (6%) and **7** (9%), we found it advantageous to perform an *i*PrOH quench instead of the mesitylation step. All three compounds **6–8** contain a B_2,N_2-pentacene fragment analogous to $\mathbf{2}^{\mathbf{Mes}}$, which presumably originates again from a rearrangement of two azasilaanthryl substituents. The third Ar_2N moiety is incorporated into the main π system through twofold intramolecular borylation (red bonds in Scheme 3). In the case of **8**, the third $SiMe_2$/BBr exchange was also successful, and the resulting bromoborane persisted until the kinetically stabilizing Mes substituent was introduced. To rationalize the formation of **6** and **7**, the following points need to be considered: (i) azasilaanthracenes in general and **5** in particular can be handled under ambient atmosphere without decomposition. It is therefore unlikely that **6** and **7** were generated by protodesilylation and oxidative $SiMe_2$ extrusion, respectively. (ii) Similar to the $\mathbf{1} \rightarrow \mathbf{3}^{\mathbf{Mes}}$ conversion, treatment of **5** with BBr_3 at room temperature, followed by mesitylation, gave $\mathbf{9}^{\mathbf{Mes}}$ in 56% yield (Scheme 3). (iii) A ^{1}H NMR spectrum recorded on the above-mentioned red precipitate after removal of all volatiles showed no signals assignable to residual SiMe groups (CD_2Cl_2; Fig. S7†). (iv) Moreover, the spectrum did not contain the characteristic proton resonances of **6** and **7** (Fig. S7†), indicating that **6** and **7** are only produced during mesitylation/*i*PrOH quenching. This process is presumably promoted by the formation of tetracoordinated boron intermediates,[23] which undergo either protodeborylation or reductive elimination at the B(III) center.

In contrast to $\mathbf{2}^{\mathbf{Mes}}$, which is synthesized most efficiently through C–H borylation of the diaminobenzene **4**, **6** and **8** are not accessible starting from the corresponding triaminobenzene 1,3,5-$(Ph_2N)_3C_6H_3$ and BBr_3 at temperatures below 200 °C. Instead, a literature-known B,N_3-PAH is generated, which is formally derived from **6** by replacing one C_3B fragment with three C–H moieties (see the ESI† for more details).[24]

The NMR spectra of **6–8** show the following characteristic features: (i) a doublet at $\delta(^1H)$ = 8.31 (2H), assignable to the two extra protons of **6**, (ii) a sharp ^{13}C resonance at 125.4 ppm for the quaternary atoms constituting the central C–C bond of the carbazole moiety in **7**, and (iii) broadened MesBC_2 signals and Mes resonances in the case of **8**.

The proposed molecular structures of **6** (Fig. S63†), **7** (Fig. S64†), and **8** (Fig. 1) were confirmed by X-ray crystallography (see the ESI† for the solid-state structures of **1**, $\mathbf{2}^{\mathbf{Br}}$, **5**, and $\mathbf{9}^{\mathbf{Mes}}$).[25] The pentacene fragments of **6–8** show only small twists with dihedral angles between the two outer 1,2-phenylene rings in the range Ar(*a*)//Ar(*b*) = 4.10(5)–13.98(4)° (see Scheme 3 for the ring labeling). Compound **6** features three [4]helicene substructures (2 × N_2,B- and 1 × B_2,N-doped) that are linked through the central benzene ring. A large dihedral angle Ar(*c*)//Ar(*d*) of 48.97(7)° is caused by steric repulsion of the two extra H atoms in the cove[26] region. Replacement of these H atoms with a C–C bond in **7** renders Ar(*c*) and Ar(*d*)

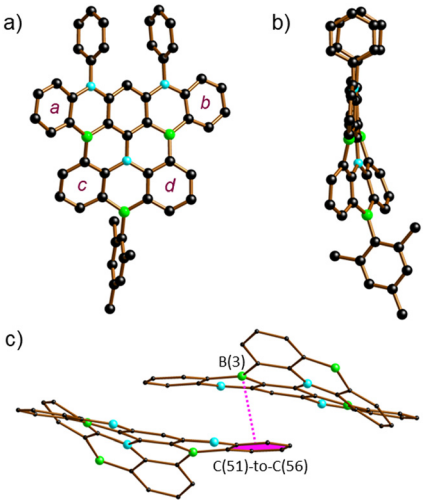

Fig. 1 Molecular structure of **8** in the solid state; (a) front view, (b) side view, and (c) section of the crystal lattice showing the pairwise π–π-stacking. H atoms are omitted for clarity; in (c), the Mes and Ph substituents are also omitted. B: green, C: black, N: cyan.

essentially coplanar. Concomitantly, the substantial dihedral angles Ar(*a*)//Ar(*c*) and Ar(*b*)//Ar(*d*) of avg. 29.41° in **6** are reduced to values of 3.43(5)–17.99(4)° in **7**. Once Ar(*c*) and Ar(*d*) are not connected by a direct C–C bond but by a BMes bridge, the reduced contraction and increased conformational flexibility in the newly formed BNC_4 ring restores the helicity in **8** with angles Ar(*a*)//Ar(*c*) and Ar(*b*)//Ar(*d*) of avg. 29.01° and Ar(*c*)//Ar(*d*) of 23.57(15)°. In the crystal lattice, the molecules of **8** are pairwise connected by π–π-stacking interactions with an off-set geometry (Fig. 1c). The intradimer distance between the B(3) atom and the C_6H_4 plane C(51)-to-C(56) is 3.403(4) Å (see pink dashed line in Fig. 1c). The $(\mathbf{8})_2$ dimers are arranged into infinite one-dimensional arrays with shortest interdimer contacts of 3.610(3) Å (Fig. S67†).

Of the molecules **6–8**, only **8** represents a new structural motif, while derivatives of **6** and **7** with alkyl and/or aryl substituents have already been reported.[22,27,28] However, the series of maximally comparable compounds **6–8** now makes it possible to study the effects of intramolecular linking (by a C–C bond or a BMes bridge) on the optoelectronic properties of the core structure **6** without the result being influenced by subtle effects of peripheral groups.

Cyclic voltammograms of $\mathbf{2}^{\mathbf{Mes}}$ and **6–8** showed a reversible first (least cathodic) reduction wave in all four cases (THF, $[n\mathrm{Bu_4N}][PF_6]$, *vs.* FcH/FcH^+; Fig. S53–S57†). The B_2,N_2-PAH $\mathbf{2}^{\mathbf{Mes}}$ is the worst electron acceptor with $E_{1/2}$ = −2.60 V (Table 1). The B_2,N_3-PAH **6** is easier to reduce by 40 mV. Here, the higher degree of delocalization seems to outcompete the presence of a formally π-electron-rich third N atom. The increased planarity of **7** due to the presence of a direct C–C bond further improves the electron-accepting ability by 210 mV. Finally, the presence of a third B(sp^2) center in the B_3,N_3-PAH **8** facilitates reduction to the largest extent ($E_{1/2}$ = −2.19 V). The general trend found for the experimentally deter-

Table 1 Selected electrochemical and photophysical data of **6**, **7**, **8**, $\mathbf{9}^{Mes}$, and $\mathbf{2}^{Mes}$, measured in THF

	$E_{1/2}$ [a] [V]	λ_{abs} [b] [nm]	λ_{em} [nm]	Φ_{PL} [c] [%]	FWHM [d] [eV]
6	−2.56	424	447	18	0.22
7	−2.35	456	479	84	0.19
8	−2.19	461	493	84	0.20
$\mathbf{9}^{Mes}$	−2.72	388	398	96	0.23
$\mathbf{2}^{Mes}$	−2.60	419	440	66	0.18

[a] THF, [nBu$_4$N][PF$_6$], *vs.* FcH/FcH$^+$. [b] Only the most bathochromically shifted absorption band is given. [c] Quantum yields were determined by using a calibrated integrating sphere. [d] Full-width at half-maximum.

mined redox potentials is consistent with the trend in the calculated LUMO-energy levels (Table S7†).

Absorption and emission spectra were recorded in THF. Compound **6** has its longest-wavelength absorption maximum and its emission maximum at λ_{abs} = 424 nm and λ_{em} = 447 nm (Fig. 2 top, Table 1). The presence of the C–C bond in **7** results in pronounced bathochromic shifts of $\Delta\lambda_{abs}$ = 0.20 eV and $\Delta\lambda_{em}$ = 0.18 eV. In comparison, the effect of an introduced BMes bridge (**8** *vs.* **6**) is even larger with band shifts of $\Delta\lambda_{abs}$ = 0.23 eV and $\Delta\lambda_{em}$ = 0.26 eV. While **6** shows a moderate photoluminescence quantum yield of Φ_{PL} = 18%, **7** and **8** have large Φ_{PL} values of 84%. We attribute the lower Φ_{PL} of **6** to two possible reasons: (i) the larger singlet–triplet (S_1–T_1) spin–orbit coupling (SOC) of **6** compared to **7** and **8** (see below) could lead to a faster intersystem crossing process and potentially generate a large population of the non-emissive triplet state. (ii) The ready inversion of the B$_2$,N-[4]helicene subunit of **6** should open efficient non-radiative decay channels.

A comparison of the approximately isomeric B$_3$,N$_3$-PAHs $\mathbf{9}^{Mes}$ and **8** reveals that the rearrangement-induced expansion of the π-electron system causes a huge bathochromic shift of the absorption and emission bands by 0.51 and 0.61 eV, respectively (Fig. 2 bottom, Table 1). The B$_2$,N$_2$-PAH $\mathbf{2}^{Mes}$ adopts an intermediate position with λ_{abs} = 419 nm and λ_{em} = 440 nm.

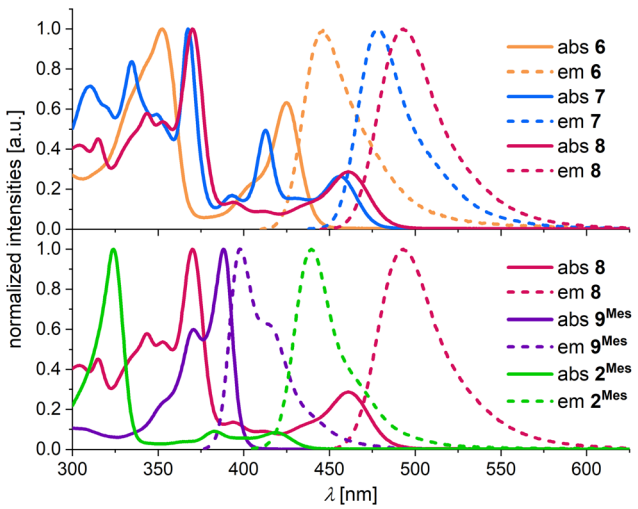

Fig. 2 Normalized UV/vis absorption and emission spectra of **6** (orange), **7** (blue), **8** (red), $\mathbf{9}^{Mes}$ (purple), and $\mathbf{2}^{Mes}$ (green), measured in THF.

Importantly, the full-width at half-maximum values (FWHM; Table 1) measured for the emission bands of all synthesized compounds meet the standards expected for MR-TADF emitters.[29] Furthermore, the transient emission-decay curves of the most extended π-electron systems **6–8** show both prompt (range: 4.2–14.8 ns) and delayed components (range: 35–136 μs; poly(methyl methacrylate) (PMMA) matrix, 0.1 wt% of the respective emitter, 300 K; Table S1†), suggesting TADF behavior.

Further insight into key excited-state properties of **6–8** and $\mathbf{2}^{Mes}$ was gained by quantum-chemical calculations using the spin-component scaling second-order algebraic-diagrammatic construction (SCS-ADC(2)) method together with the def2-SVP basis set. For all four compounds, we find that the lowest excited singlet state (S_1) is mostly described by a HOMO → LUMO transition (>70% weight) with considerable oscillator strength (f > 0.1; Table S8 and Fig. S69†). The trend in computed S_1 energies follows the one experimentally observed in the electronic spectra, with a decrease in energy along the sequence $\mathbf{2}^{Mes}$ → **6** → **7** → **8**. The lowest excited triplet state (T_1) is also predominantly described by a HOMO → LUMO transition for all compounds except for molecule **6**, where T_1 is mainly described by a HOMO → LUMO+1 transition (85% weight). In addition, all molecules exhibit short-range charge-transfer (SRCT) excited states that are characterized by an alternating pattern of increasing and decreasing electron density on adjacent atoms, which is a typical feature of multiple resonance TADF compounds. The CT character of an excited state can be quantified by analyzing the CT distance (d_{CT}) between the positive and negative electron density variation ($\Delta\rho$) and the charge transferred upon excitation (q_{CT}). The computed d_{CT} for **6** has the lowest value of ≈0.80 Å for both the S_1 and the T_1 state; d_{CT} increases to 2.35 Å (1.86 Å) for S_1 (T_1) in **7** and 2.45 Å (2.13 Å) for S_1 (T_1) in **8**, likely due to increased π conjugation (Table S9†). These results point toward a larger CT character for **7** and **8** as compared to **6**. For $\mathbf{2}^{Mes}$, d_{CT} is intermediate [S_1 (T_1): 1.85 Å (1.63 Å)]. Excited states with large q_{CT} and/or large d_{CT} are expected to be more strongly influenced by solvent effects. In line with this expectation and the computed d_{CT} values, a comparison of the calculated gas-phase emission spectra and our experimentally obtained spectra (THF, relative permittivity ε = 7.58 at T = 298.15 K)[30] shows the smallest solvent-induced red-shift for **6**, followed by $\mathbf{2}^{Mes}$, **7**, and **8** (Fig. S70† and Table 1). The vertical energy gap between the S_1 and T_1 states (ΔE_{ST}) is predicted to be small for compounds **6** (0.06 eV), **7** (0.15 eV), and **8** (0.12 eV), but slightly larger for $\mathbf{2}^{Mes}$ (0.27 eV; Table S8†). The adiabatic ΔE_{ST} values do not change much compared to the vertical ones for compounds **7** (0.15 eV), **8** (0.12 eV), and $\mathbf{2}^{Mes}$ (0.34 eV; Table S10†). A more pronounced change from 0.06 to 0.20 eV is computed for **6** (Table S10†) as a consequence of the different nature of its S_1 and T_1 states, which leads to an asymmetric relaxation toward the minima of their respective potential energy surfaces. Our

computed adiabatic ΔE_{ST} values are in line with experimentally determined data for derivatives of **6** (0.18 eV) and **7** (0.11 eV).[15,22,27] To further elaborate on a possible (reverse) intersystem-crossing [(r)ISC] mechanism, we emphasize that the computed spin–orbit coupling (SOC) between the S_1 and T_1 states of **6** is as large as 0.662 cm^{-1}, and thus about one order of magnitude higher than the SOCs of **7**, **8**, and $\mathbf{2}^{\mathbf{Mes}}$ (Table S11†). As the (r)ISC rate constant is proportional to the SOC,[31] the lower Φ_{PL} of **6** can be rationalized by a high ISC rate that successfully competes with the rate of radiative decay. We hypothesize that, despite the large SOC, the rISC rate might be limited by the high ΔE_{ST}, thereby hampering triplet upconversion. Interestingly, the second excited triplet state T_2 is very close in energy to the S_1 state in **6** (Δ = 0.01 eV), **7** (Δ = −0.01 eV), and $\mathbf{2}^{\mathbf{Mes}}$ (Δ = 0.01 eV), whereas this energy gap is larger in **8** (Δ = 0.16 eV). Furthermore, the SOC between the S_1 and T_2 states is comparable to the SOC between S_1 and T_1 for $\mathbf{2}^{\mathbf{Mes}}$ and **7**, but larger (smaller) for **8** (**6**). The reason lies in the fact that S_1 and T_2 of **8** (**6**) have different (similar) electron-density distribution patterns, as can be seen in the difference-density plots between S_1–T_1 and S_1–T_2 (Fig. 3). In view of the SOC values and the energy difference of T_2 relative to S_1, we propose that T_2 could play a major role for the emission behavior of compounds **7** and **8**, but less so for that of **6**. In the case of compound $\mathbf{2}^{\mathbf{Mes}}$, both the S_1–T_1 and T_1–T_2 energy gaps (≈0.3 eV) are quite large, thereby limiting reverse intersystem crossing and supporting the observed absence of delayed fluorescence for this compound.

The vibronically resolved absorption and emission spectra of **6–8** and $\mathbf{2}^{\mathbf{Mes}}$ were simulated within the Franck–Condon approximation using the normal modes computed at the time-dependent density functional (TD-DFT) level (see the ESI† for further details). As can be seen in Fig. S70a,† the experimentally observed trend in the energy of the most bathochromic absorption peak is well reproduced by the S_1 vertical excitation energy computed from the optimized ground-state structure (Table S8†). The FWHM values obtained from the simulation of the emission spectra (0.24 eV (31 nm) for **6**, 0.20 eV (26 nm) for **7**, 0.21 eV (28 nm) for **8**, and 0.19 eV (23 nm) for $\mathbf{2}^{\mathbf{Mes}}$; Fig. S70b†) are in excellent agreement with the experiments (Table 1). Moreover, the FWHMs are rather small, in line with the small computed reorganization energies of around 0.1 eV, highlighting the rigidity of all compounds (see Fig. S71†). Apart from molecule **7** whose emission spectrum is broadened by both low-frequency and high-frequency modes, the emission spectra of the other molecules are mainly broadened by low-frequency modes (see Huang–Rhys factor plot in terms of the frequency in Fig. S72†).

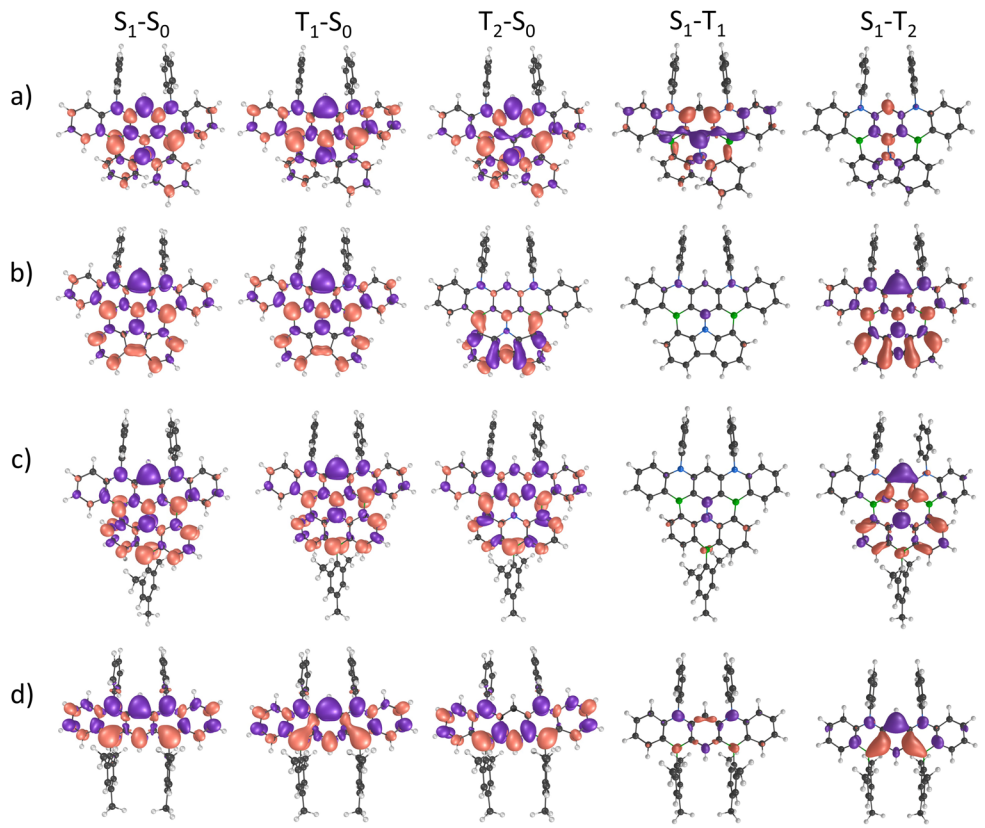

Fig. 3 Difference-density plots between the excited states (S_1, T_1, and T_2) and the ground state (S_0) for (a) **6**, (b) **7**, (c) **8**, and (d) $\mathbf{2}^{\mathbf{Mes}}$ calculated at the SCS-ADC(2)/def2-SVP level. An isovalue of 0.001 e au^{-3} was used to plot the densities.

Conclusions

1,3- and 1,3,5-azasilaanthryl-substituted benzenes (**1** and **5**) contain only small, locally constrained π-conjugated systems, due to their sterically enforced propeller-type conformations. We have now demonstrated that a one-pot sequence of Si/B exchange, skeletal rearrangement, and electrophilic borylation reactions leads from **1** or **5** to B_n,N_m-doped nanographenes with extended π-electron clouds. The series of closely related products (**6–8**) enabled us to elucidate the profound effects of linking peripheral aryl fragments in **6** by either a direct C–C bond (**7**) or a borylene bridge (**8**). Apart from substantial structural changes (**6** is a trifold [4]helicene whereas **7** is essentially planar), especially the optoelectronic properties are affected: upon going from **6** to **8**, electrochemical reduction becomes more facile by 0.37 V; the most bathochromic absorption band and the emission band shift from 424 nm to 461 nm and from 447 nm to 493 nm, respectively. The distribution of the π-electron-accepting B atoms and the π-electron-donating N atoms in the individual polycyclic aromatic hydrocarbons fulfils the formal prerequisite for multiple resonance thermally activated delayed fluorescence (MR-TADF). Indeed, the transient emission-decay curves of **6–8** show a delayed component and quantum-chemical calculations reveal short-range charge-transfer excited states with alternating patterns of increasing and decreasing electron density on adjacent atoms. The energy gaps between the S_1 and T_1 states (ΔE_{ST}) are predicted to be small (≤0.2 eV). Also, the computed spin–orbit coupling between the S_1 and T_1 states of **6–8** is appreciably high. In summary, we herein disclose a straightforward route to potentially useful, energy-efficient OLED emitters.

Author contributions

E. Z. carried out all compound syntheses, characterizations of new compounds, and quantum-chemical calculations of $\mathbf{2}^{\mathbf{Br}}$ and $\mathbf{3}^{\mathbf{Br}}$. All other computational studies were performed by D. V. and Y. O.; R. N. assisted with the synthesis of $\mathbf{2}^{\mathbf{Mes}}$, $\mathbf{2}^{\mathbf{Br}}$, and $\mathbf{3}^{\mathbf{Mes}}$. S. K. assisted with the synthesis of **1**, **5**, and $\mathbf{9}^{\mathbf{Mes}}$. M. B. performed the X-ray crystal structure analysis of $\mathbf{2}^{\mathbf{Br}}$. A. V. performed the X-ray crystal structure analyses of all other compounds. H.-W. L., Y. O., and M. W. supervised the project. The manuscript was written by E. Z., D. V., Y. O., and M. W. and edited by all co-authors.

Conflicts of interest

There are no conflicts to declare.

Acknowledgements

Parts of this research (project I-20220822) were carried out at PETRA III at DESY (Hamburg), a member of the Helmholtz Association (HGF). We would like to thank Dr Martin Tolkiehn and Dr Eugenia Peresypkina for their assistance regarding the use of the beamline P24 at DESY. We also wish to thank Prof. Dr Thomas Jüstel and Dr David Enseling from the University of Applied Sciences Münster, Department of Chemical Engineering for the photoluminescence decay and emission measurements in PMMA. D. V. and Y. O. acknowledge funding from Fonds de la Recherche Scientifique-FNRS under grant no. F.4534.21. This research used resources of the "Plateforme Technologique de Calcul Intensif (PTCI)" (**https://www.ptci.unamur.be**) located at the University of Namur, Belgium, which is supported by the FNRS-FRFC, the Walloon Region, and the University of Namur (conventions no. 2.5020.11, GEQ U.G006.15, 1610468, RW/GEQ2016 et U.G011.22). The PTCI is member of the "Consortium des Équipements de Calcul Intensif (CÉCI)" (**https://www.ceci-hpc.be**).

References

1 I. Shin, H. N. Lim and W. P. Hong, *Synthesis*, 2022, **54**, 570–588.
2 T. Hatakeyama, K. Shiren, K. Nakajima, S. Nomura, S. Nakatsuka, K. Kinoshita, J. Ni, Y. Ono and T. Ikuta, *Adv. Mater.*, 2016, **28**, 2777–2781.
3 Y. Kondo, K. Yoshiura, S. Kitera, H. Nishi, S. Oda, H. Gotoh, Y. Sasada, M. Yanai and T. Hatakeyama, *Nat. Photonics*, 2019, **13**, 678–682.
4 Y. Sano, T. Shintani, M. Hayakawa, S. Oda, M. Kondo, T. Matsushita and T. Hatakeyama, *J. Am. Chem. Soc.*, 2023, **145**, 11504–11511.
5 R. K. Konidena and K. R. Naveen, *Adv. Photonics Res.*, 2022, **3**, 2200201.
6 S. M. Suresh, D. Hall, D. Beljonne, Y. Olivier and E. Zysman-Colman, *Adv. Funct. Mater.*, 2020, **30**, 1908677.
7 F. Huang, X.-C. Fan, Y.-C. Cheng, H. Wu, X. Xiong, J. Yu, K. Wang and X.-H. Zhang, *Angew. Chem., Int. Ed.*, 2023, **62**, e202306413.
8 T. Hua, J. Miao, H. Xia, Z. Huang, X. Cao, N. Li and C. Yang, *Adv. Funct. Mater.*, 2022, **32**, 2201032.
9 S. Oda, B. Kawakami, Y. Yamasaki, R. Matsumoto, M. Yoshioka, D. Fukushima, S. Nakatsuka and T. Hatakeyama, *J. Am. Chem. Soc.*, 2022, **144**, 106–112.
10 X. Lv, J. Miao, M. Liu, Q. Peng, C. Zhong, Y. Hu, X. Cao, H. Wu, Y. Yang, C. Zhou, J. Ma, Y. Zou and C. Yang, *Angew. Chem., Int. Ed.*, 2022, **61**, e202201588.
11 H. J. Cheon, Y.-S. Shin, N.-H. Park, J.-H. Lee and Y.-H. Kim, *Small*, 2022, **18**, 2107574.
12 X.-C. Fan, F. Huang, H. Wu, H. Wang, Y.-C. Cheng, J. Yu, K. Wang and X.-H. Zhang, *Angew. Chem., Int. Ed.*, 2023, **62**, e202305580.
13 E. Zender, S. Karger, R. Neubaur, A. Virovets, H.-W. Lerner and M. Wagner, *Org. Lett.*, 2024, **26**, 939–944.
14 M. Yang, I. S. Park and T. Yasuda, *J. Am. Chem. Soc.*, 2020, **142**, 19468–19472.
15 M. Mamada, M. Hayakawa, J. Ochi and T. Hatakeyama, *Chem. Soc. Rev.*, 2024, **53**, 1624–1692.

16 Y. Liu, X. Xiao, Z. Huang, D. Yang, D. Ma, J. Liu, B. Lei, Z. Bin and J. You, *Angew. Chem., Int. Ed.*, 2022, **61**, e202210210.
17 P. Jiang, L. Zhan, X. Cao, X. Lv, S. Gong, Z. Chen, C. Zhou, Z. Huang, F. Ni, Y. Zou and C. Yang, *Adv. Opt. Mater.*, 2021, **9**, 2100825.
18 C. M. van Beek, A. M. Swarbrook, C. E. Creissen, C. S. Hawes, T. A. Gazis and P. D. Matthews, *Chem. – Eur. J.*, 2024, **30**, e202301944.
19 T. Agou, J. Kobayashi and T. Kawashima, *Org. Lett.*, 2006, **8**, 2241–2244.
20 For corresponding B_3,N_3-heptacenes, see: (*a*) S. M. Suresh, E. Duda, D. Hall, Z. Yao, S. Bagnich, A. M. Z. Slawin, H. Bässler, D. Beljonne, M. Buck, Y. Olivier, A. Köhler and E. Zysman-Colman, *J. Am. Chem. Soc.*, 2020, **142**, 6588–6599; (*b*) K. Stavrou, S. M. Suresh, D. Hall, A. Danos, N. A. Kukhta, A. M. Z. Slawin, S. Warriner, D. Beljonne, Y. Olivier, A. Monkman and E. Zysman-Colman, *Adv. Opt. Mater.*, 2022, **10**, 2200688.
21 J. A. Knöller, G. Meng, X. Wang, D. Hall, A. Pershin, D. Beljonne, Y. Olivier, S. Laschat, E. Zysman-Colman and S. Wang, *Angew. Chem., Int. Ed.*, 2020, **59**, 3156–3160.
22 C–N-bond cleavage reactions in comparable systems have been reported: K. Matsui, S. Oda, K. Yoshiura, K. Nakajima, N. Yasuda and T. Hatakeyama, *J. Am. Chem. Soc.*, 2018, **140**, 1195–1198.
23 Precedence for such reactivity exists in the form of a 9,10-dihydro-9,10-diboraanthracene → 9-borafluorene conversion: S. Kirschner, S.-S. Bao, M. K. Fengel, M. Bolte, H.-W. Lerner and M. Wagner, *Org. Biomol. Chem.*, 2019, **17**, 5060–5065.
24 Y. Wang, Y. Duan, R. Guo, S. Ye, K. Di, W. Zhang, S. Zhuang and L. Wang, *Org. Electron.*, 2021, **97**, 106275.
25 Compound **6** crystallizes with 0.25 toluene solvate molecules. The crystal lattice contains two molecules **6A** and **6B** in the asymmetric unit; since the key metrical parameters of **6A** and **6B** are sufficiently similar considering the experimental error margins (*cf.* the overlay in Fig. S63b†), it is justified to discuss only the data of **6A** in the main text. Compound **7** crystallizes as a C_6H_6 solvate with two crystallographically unique molecules, **7A** and **7B**, in general positions. Some key metrical parameters of **7A** and **7B** differ significantly, so both molecules are considered in the discussion whenever necessary. Compound **8** crystallizes with two $CHCl_3$ solvate molecules.
26 R. Rieger and K. Müllen, *J. Phys. Org. Chem.*, 2010, **23**, 315–325.
27 S. Oda, W. Kumano, T. Hama, R. Kawasumi, K. Yoshiura and T. Hatakeyama, *Angew. Chem., Int. Ed.*, 2021, **60**, 2882–2886.
28 T. Hatakeyama, A. Mizutani and T. Koike, WO2017188111A1, 2017.
29 During borylation experiments on $\mathbf{3}^{\mathbf{Mes}}$ with BBr_3 in C_6D_6, we observed essentially quantitative H/D exchange at the positions *ortho* and *para* to the N atoms, while exchange at the *meta* positions was far less pronounced (see the ESI† for more details). This can be considered as an experimental mapping of the charge-density distribution in the HOMO of $\mathbf{3}^{\mathbf{Mes}}/\mathbf{2}^{\mathbf{Br}}$.
30 J. F. Coetzee and T.-H. Chang, *Pure Appl. Chem.*, 1985, **57**, 633–638.
31 Y. Olivier, B. Yurash, L. Muccioli, G. D'Avino, O. Mikhnenko, J. C. Sancho-García, C. Adachi, T.-Q. Nguyen and D. Beljonne, *Phys. Rev. Mater.*, 2017, **1**, 075602.